Charge ordering as the driving mechanism for superconductivity in rare-earth nickel oxides

Álvaro Adrián Carrasco Álvarez,[1,2] Lucia Iglesias,[2] Sébastien Petit,[1] Wilfrid Prellier,[1] Manuel Bibes,[2] and Julien Varignon[1]
[1]*CRISMAT, ENSICAEN, Normandie Université, UNICAEN, CNRS, 14000 Caen, France*
[2]*Unité Mixte de Physique, CNRS, Thales, Université Paris Saclay, 91767 Palaiseau, France*

(Received 9 May 2023; revised 5 February 2024; accepted 10 April 2024; published 4 June 2024)

Superconductivity is one of the most intriguing properties of matter, described by an attractive interaction that binds electrons into Cooper pairs. To date, the highest critical temperature at ambient conditions is achieved in copper oxides. While layered nickel oxides were long proposed to be analogous to cuprates, superconductivity was only demonstrated in 2019 albeit without clarifying the pairing mechanism. Here we use density functional theory to show that superconductivity in nickelates is driven by an electron-phonon coupling originating from a charge ordering. Due to an intrinsic electronic instability in half-doped compounds, $Ni^{1.5+}$ cations dismutate into more stable Ni^{+} and Ni^{2+} cations, which is accompanied by a bond disproportionation of NiO_4 complexes producing an insulating charge-ordered state. Once doping suppresses the instability, the bond disproportionation vibration is sufficient to reproduce the key characteristic of nickelates observed experimentally, notably the dome of T_c as a function of doping content. These phenomena are identified if relevant degrees of freedom as well as an exchange-correlation functional that sufficiently amends self-interaction errors are involved in the simulations. Finally, despite the presence of correlation effects inherent to $3d$ elements that favor the formation of local Ni spins, the mechanism behind the formation of Cooper pairs in nickelate superconductors appears similar to that of nonmagnetic bismuth oxide superconductors.

DOI: 10.1103/PhysRevMaterials.8.064801

I. INTRODUCTION

Superconductivity is a peculiar property of materials characterized by zero electrical resistance to direct current and perfect diamagnetism, thereby offering numerous applications. This state is explained on the basis of an attractive interaction binding electrons into Cooper pairs [1]. The most famous superconductors are the cuprates that set the record for the critical temperature T_c(∼138 K) at ambient conditions [2]. However, the identification of the pairing mechanism in these compounds has been hindered by the absence of analogs. In this regard, it was long proposed that nickel oxides could host superconductivity due to their proximity with copper in the periodic table [3,4]. These efforts recently crystallized in the infinitely layered phase $R$$NiO_2$ [5–8] and a reduced phase of the Ruddlesden-Popper series, $R_{n+1}Ni_nO_{2n+2}$ ($n = 5$) [9], where R is a trivalent rare earth, thereby offering an alternative playground to understand pairing mechanisms in oxide superconductors.

Superconducting nickelates adopt the chemically reduced Ruddlesden-Popper (RRP) structure $R_{n+1}Ni_nO_{2(n+1)}$, where the most studied case is the limit member $n = \infty$ (called the infinitely layered phase $R$$NiO_2$) [Fig. 1(a)]. These nickelates are based on NiO_2 planes [Fig. 1(a)] stacked along the c axis and separated by layers of rare earth R. The motif is then sandwiched with two RO_2 fluorite slabs, except when $n = \infty$, for which only R cations are intercalated between the NiO_2 planes. This layered structure of NiO_2 planes is common to several oxide superconductors such as cuprates [2], ruthenates (Sr_2RuO_4) [10], and iridates (Sr_2IrO_4) [11,12].

Gathering the experimental data from the literature regarding the T_c versus Ni $3d$ electron count [Fig. 1(b)], it becomes clear that superconductivity emerges in a narrow Ni valency region centered at a $3d^{8.8}$ occupancy. This strongly suggests that the Ni valency is the determining factor in the transition toward the superconducting (SC) phase. Most studies in the literature focus on how transiting from the $n = \infty$ member to the SC region is accomplished by hole doping the material [14–22]. However, these $n = \infty$ nickelates are experimentally found to be bad metals [5], as also found by our density functional theory (DFT) calculations (see Fig. S1 in Supplemental Material [23]). This strategy is quite surprising, and it is at odds with the usual procedure to reach the SC region in several oxide superconductors, such as cuprates, bismuthates, and antimonates, where doping induces the transition from an insulating state to a metallic, superconducting phase.

This apparent contradiction is alleviated if one reads the phase diagram of Fig. 1(b) starting from the $n = 1$ member. In that regard, studying the electronic properties of La_2NiO_4, we find it to be a robust Mott insulator at the DFT level with a large band gap of 2 eV (see Fig. S1 in Supplemental Material [23]). Thus, reaching the superconducting phase starting from La_2NiO_4 requires doping a Mott insulator with electrons. Therefore, one may ask if one can interpret the superconducting phase of nickelates from the point of view of electron doping of Mott insulators instead of hole doping metals. If this is true, then can we get insights on the superconducting mechanism in these nickel oxide superconductors? For instance, is there any intrinsic instability in the doped phase diagram of these nickelates?

In this article, we reveal, on the basis of DFT simulations, the existence of a charge-ordered (CO) insulating state at half doping. The CO state is a consequence of an unstable 1.5+ formal oxidation state (FOS) of Ni cations that prefer

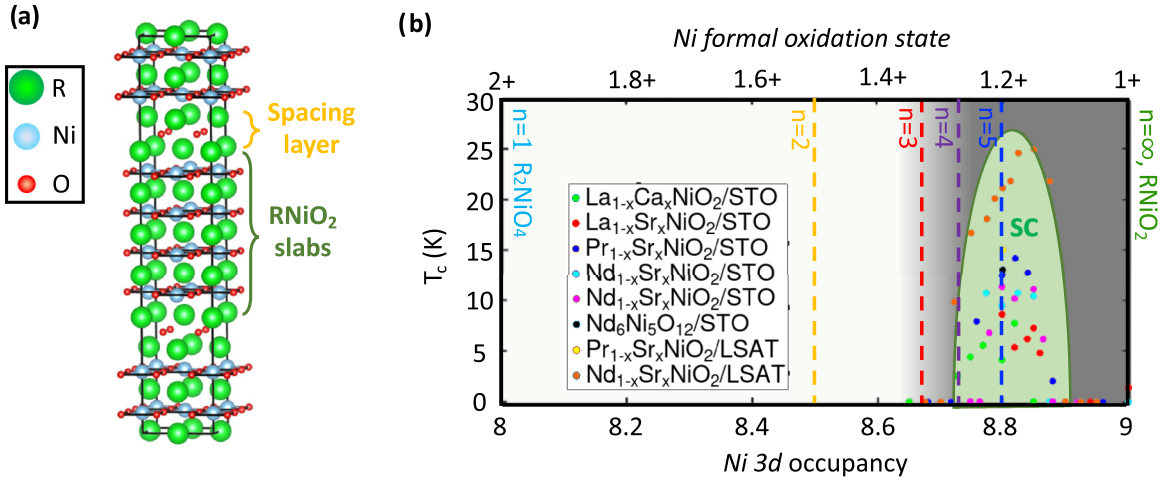

FIG. 1. Structural and electronic properties of nickelates. (a) Reduced Ruddlesden-Popper (RPP) phase exhibited by nickelates consisting of n RNiO$_2$ slabs intercalated between spacing layers. (b) Critical temperature T_c (in kelvin) of rare-earth nickelates versus the Ni $3d$ electron count extracted from experimental results available in literature. Experimental critical temperatures T_c are taken from Refs. [5–9,13].

to adopt the 1+ and 2+ FOS in the ground state, either as a RRP $n = 2$ or as a $La_{0.5}Sr_{0.5}NiO_2$ infinitely layered structure. The CO phase is accompanied by a bond disproportionation, producing compressed and extended O_4 complexes. Using this insulating state as a starting point, we then reveal that doping the material with electrons progressively suppresses the instability toward disproportionation effects. Then, the distortion is completely suppressed once we reach an effective Ni valency of 8.75, reminiscent of the valency required to reach the SC state experimentally. Thus, it appears that the SC state is in the vicinity of a charge-ordered state, in close similarity to bismuth and antimony oxide superconductors [24–27]. When the metallic state is reached, we then show that the disproportionation vibration is sufficient to reproduce the experimentally observed critical temperatures of $La_{1-x}Sr_xNiO_2$. Thus, superconductivity is dominated by an electron-phonon coupling in these nickelates, despite the presence of correlation effects inherent to transition metal cations. All these results are obtained by involving all relevant degrees of freedom, such as structural lowering events and local spin formation, as well as an appropriate exchange-correlation functional. Most notably, the usual non-spin-polarized (nonmagnetic, or NM) solution is shown to fail at capturing the bond disproportionation effects and to produce energy solutions at least 150 meV (i.e., 1800 K) greater than solutions with an appropriate paramagnetic representation of Ni spin interactions.

II. METHODOLOGY

Prior to discussing the physical properties of electron-doped nickelates, it is relevant to discuss several critical elements of the first-principles simulations. The literature abounds with DFT-based studies of the superconducting nickelates using a non-spin-polarized (NM) solution, with symmetry conserving undistorted cells and/or in combination with a poor description of exchange-correlation (xc) phenomena, such as involving local density approximation (LDA) or generalized gradient approximation (GGA) density functionals. These critical points notably led to rule out an electron-phonon coupling in RNiO$_2$ from a combination of NM-GGA calculations in Ref. [15] and DFT-LDA in Ref. [28], the latter highlighting the importance of treating correlation effects at the prohibitive Green's function level. The reason behind these shortcuts comes from limited possibilities for computing the full electron-phonon coupling from first-principles simulations: (i) theoretical tools can only be performed at a non-spin-polarized level so far and (ii) the calculation is far too demanding in terms of computational resources to include an appropriate xc functional and allow symmetry-lowering events (larger cell with less symmetry). Although fantastic tools for computing electron-phonon response in nonmagnetic systems with weakly correlated features, existing codes are not, however, suited for studying complex oxide systems involving transition metal elements. Notably, Ref. [29] demonstrated that LDA-GGA xc functionals as well as the NM approximation fall outside the appropriate possibilities for describing properties of transition metal oxide materials. Finally, as we discuss below, a practical implementation for estimating superconducting quantities with band-structure techniques goes through the estimation of band splitting associated with given lattice distortions and/or vibrations. Within this procedure, superconducting quantities are related to quantification of band splitting and hence are extremely sensitive to the choice of the DFT xc functional.

Superconducting properties. We have calculated the reduced electron-phonon matrix element (REPME) associated with a B_{oc} distortion by freezing its atomic displacement in the relaxed ground state. Using the band splitting ΔE_k appearing in the band structure at the k coordinate in the first Brillouin zone due to the frozen phonon displacement, we compute the REPME by using the formula $D = \frac{\Delta E_k}{2u}$, where u is the displacement of one O atom for the condensed phonon mode—if it does involve only O motions. This standard procedure was successful in $BaBiO_3$, $SrBiO_3$, and MgB_2 compounds [26,30,31]. In order to calculate the electron-phonon coupling λ, we use the formula $\lambda = N(E_F)\frac{\hbar^2}{2M\omega_B^2}D^2$, where $N(E_F)$ is the density of states at the Fermi level per spin channel and per formula unit, M is the mass of the moving ion in the phonon mode, and ω_B is the frequency of the B_{oc} phonon mode. To

obtain the critical temperature T_c, we use the McMillan-Allen equation [32], $T_c = \frac{\omega_{\log}}{1.12}\exp(\frac{-1.04(\lambda+1)}{\lambda-\mu^*(1+0.62\lambda)})$, where $\omega_{\log}$ is the logarithmic averaged phonon frequency (expressed in kelvin) and μ^* is the screened Coulomb potential with conventional values ranging from 0.1 to 0.15.

The choice of the DFT xc functional. LDA and GGA cannot sufficiently amend self-interaction errors inherent to practiced DFT, particularly for 3*d* transition metal elements. Therefore, it usually yields metals, while most 3*d* transition metal compounds are insulators experimentally [29,33]. Since the practical implementation for estimating superconducting quantities relies on the estimation of band splitting in band structures in the present study, it should be modeled with care. Involving more evolved DFT functionals such as meta-GGA or hybrid may help to describe accurately the electronic features and superconducting properties. This was already highlighted in Refs. [26,30]. In this study, most simulations are performed with the strongly constrained and appropriately normalized (SCAN) meta-GGA functional [34]. This functional is able to predict the correct trends in lattice distortions and metal-insulator transitions in bulk ABO_3 perovskite oxides and trends in doping effects in nickelates and bismuthates [26,33,35]. In addition, SCAN does not require any external parameter as in DFT+U and hence is able to adapt to different oxidation states of ions as a result of doping or the appearance of charge orderings. However, this functional may underestimate the band gap of these strongly correlated nickel oxides with a low nominal valence—the lower the formal oxidation state, the larger the self-interaction errors [36]—as in highly uncorrelated semiconductors. We have thus benchmarked our DFT SCAN results by performing one-shot simulations on smaller nickelate systems with a hybrid HSE06 [37] functional to evaluate the enhancement of band splitting, in the spirit of Ref. [30]. Although the hybrid functionals can sometimes overlocalize electrons and open band gaps in materials that are metals experimentally such as in the doped cuprates [38,39], the HSE06 functional has been already used in the infinitely layered nickelates and was shown to preserve the metallic character of the limiting members $LaNiO_2$ and $PrNiO_2$ [36]. The standard parametrization of the HSE06 functional was used, namely, with 25% of exact Hartree-Fock exchange and a range separation of 0.2 $Å^{-1}$. We emphasize, however, that all calculations have been performed with the SCAN functional unless stated.

Local spin formation may not be overlooked. Within the NM representation, all transition metal elements are forced to have no magnetization at all, i.e., $n_\uparrow = n_\downarrow$, where n is the number of electrons with spin $\uparrow$ or $\downarrow$. This is quite surprising for elements such as Ni exhibiting a $3d^9$ configuration with a spin-unpaired electron in the infinitely layered $RNiO_2$ phase. Alternatively, one may use a supercell with a true paramagnetic order by randomizing spins at the restriction that the sum over all spins must be zero. Using this representation, we indeed identify that the energy difference between a fully relaxed NM phase and paramagnetic (PM) phase in our DFT simulations as a function of doping content in the $La_{1-x}Sr_xNiO_2$ phase diagram is massive, with at least 150 meV/f.u. of energy gain by developing a spin-polarized solution (Fig. S2 in Supplemental Material [23]). It corresponds to a NM phase that would be stable above at least at $T = 1800$ K. This value has to be compared with the 15–25 K targeted for the critical temperature T_c of superconducting nickelates. As we will show later in the paper, neglecting Hund's rule for coupling in the DFT simulation has several dramatic consequences as it prevents structural lowering events strongly coupled to electronic features and enables a totally different band-structure problem. Thus, the NM approximation is not an appropriate starting point for understanding the superconducting mechanism. Even though electron-electron interactions are treated with the highest level of description such as with DFT with hybrid functionals or by introducing a many-body Green's function, for instance, the results are dependent on the input basis, and their application on a non-spin-polarized input will only produce an improvement of the band dispersion of a non-spin-polarized system.

To circumvent potential spin-phonon couplings, we used a paramagnetic representation for Ni spins following the strategy presented in Ref. [29]. The Alloy Theoretic Automated Toolkit (ATAT) package [40] and the special quasirandom structures (SQSs) [41] are used for identifying the spin arrangement maximizing the disorder characteristic of a random spin configuration within a given supercell size, although spins are only treated at the collinear level.

Crystallographic cells, structural relaxations, and analysis. The imposed starting cells correspond to high-symmetry *P4/mmm* and the *I4/mmm* tetragonal unit cells for the $RNiO_2$ infinitely layered phases and the reduced Ruddlesden-Popper phase, respectively. Solid solutions of the infinitely layered phase correspond to $(2\sqrt{2}, 2\sqrt{2},4)$ supercells with respect to the primitive *P4/mmm* cell (32 f.u.). The RRP $n = 2$ phase is modeled by a (2,2,1) supercell, corresponding to a supercell with 176 ions. The choice of these cells is guided by their ability to accommodate lattice distortions as well as the PM solution. We then proceed to the full structural relaxation (cell parameters and shape as well as atomic positions) until the forces acting on each atom are lower than 0.05 eV/Å. The amplitudes of the distortions of the relaxed ground states are then extracted using symmetry mode analysis, taking as reference the undistorted *P4/mmm* and *I4/mmm* cells for infinitely layered and RRP phases, respectively. This is performed with the ISODISTORT tool from the ISOTROPY applications [42,43].

Doping effects in superlattices and disordered solid solutions. Doping effects are performed by substituting La^{3+} cations by Sr^{2+} divalent cations. In the disordered solid solution (DSS), the disorder characteristic of an alloy is extracted using the SQS technique developed by Zunger *et al.* [41], allowing to extract the cation arrangement maximizing the disorder and the occurrence of all possible local motifs in a given supercell size. The DSS cell size is limited to 32 f.u. in order to have a feasible calculation with PM and/or cation disorder inducing a *P1* symmetry.

Searching for electronic instabilities. The SCAN functional is a local functional of the density matrix unable to make a distinction between occupied and unoccupied states. It is therefore unable to identify electronic instabilities in high-symmetry cells with degenerate partners as performed in Ref. [29] where one has to impose integer occupancy of a specific degenerate partner such as (1,0) instead of (0.5,0.5) for two degenerate orbitals. Instead, we used the strategy proposed in Ref. [44]: we plot the potential energy surface

associated with a lattice distortion and seek to see the shape of the potential energy surface. A shifted single potential whose minimum is located at nonzero amplitude of the mode then indicates the presence of an electronic instability, as those observed for the Jahn-Teller or bond disproportionation distortions in Ref. [44].

Checks of the existence of electronic instabilities have, nevertheless, been performed on simpler systems with a ferromagnetic order of Ni spins by performing two sets of calculations on a high-symmetry undistorted cell using hybrid DFT HSE06 calculations: (i) a calculation where one enforces similar occupancies of degenerate partners and (ii) a calculation where one imposes specific orbital occupancies and switches off the symmetry on the wave function. The difference of energy between calculations (i) and (ii) then indicates the presence or absence of electronic instabilities at 0 K.

Potential energy surface and phonon frequencies. The potential energy surfaces associated with a lattice distortion labeled B are computed, taking as a reference the undistorted *P4/mmm* and *I4/mmm* for the infinitely layered and the reduced Ruddlesden-Popper phase, respectively. Then a finite distortion amplitude Q_B is frozen in the material and the energy is computed for different amplitudes. Regarding the phonon frequencies, a full phonon calculation is not affordable since the DSS formula unit supercell contains more than 100 atoms without any symmetry. Instead, we simply compute the potential energy surface of the desired distortion in the relaxed ground-state structure by freezing different mode amplitudes as proposed in Ref. [26]. Due to the presence of an electronic instability that moves the single-well minimum to nonzero amplitude of Q_B, the evolution of the energy ΔE is given by the following expression:

$$\Delta E = E_0 + \alpha(Q_B - Q_0)^2 + \beta(Q_B - Q_0)^4, \tag{1}$$

where α and β are coefficients and Q_0 signals the force acting on the electrons even in the absence of Q_B (i.e., the electronic instability). It follows that

$$\begin{aligned}\Delta E &= E_0 + \alpha Q_B^2 + \alpha Q_0^2 - 2\alpha Q_B Q_0 + \beta Q_B^4 + \beta Q_0^4 \\ &\quad -4\beta Q_B^3 Q_0 - 4\beta Q_B Q_0^3 + 6\beta Q_B^2 Q_0^2, \end{aligned}\tag{2}$$

$$\begin{aligned}\Delta E &= E_0 + \left(\alpha Q_0^2 + \beta Q_0^4\right) + \left(-2\alpha Q_0 - 4\beta Q_0^3\right) Q_B \\ &\quad + \left(\alpha + 6\beta Q_0^2\right) Q_B^2 + (-4\beta Q_0) Q_B^3 + \beta Q_B^4, \end{aligned}\tag{3}$$

$$\Delta E = E_0' + b\, Q_B + c Q_B^2 + d Q_B^3 + e\, Q_B^4, \tag{4}$$

with $E_0' = E_0 + (\alpha Q_0^2 + \beta Q_0^4)$. From Eq. (3), we recover the linear and trilinear term in Q_B signaling the contribution of the electronic instability. Using a fit of the potential energy surfaces as a function of Q_B with a polynomial expression up to the fourth order, we can extract all the coefficients of Eq. (4) and map them to get the mode frequency through the relation $\omega = \sqrt{\frac{2\alpha}{M}}$; i.e., $E_{\text{harm}} = \frac{1}{2}\text{M}\omega^2 Q_B^2$.

Other technical details. DFT simulations are performed with the Vienna *Ab initio* Simulation Package (VASP) [45,46]. Projector augmented wave (PAW) pseudopotentials [47] are used, taking the $3d^8 4s^2$, $5p^6 5d^1 6s^2$, and $4s^2 4p^6 5s^2$ electrons as valence electrons for Ni, La, and Sr atoms, respectively. The energy cutoff is set to 650 eV and is accompanied by a $3\times\ 3\times 2$ gamma-centered k mesh for the 32 f.u. supercells. The k mesh is set to $3\times\ 3\times 1$ for the RRP $n = 2$ cell (176 ions/supercell). Wannier functions are built using the WANNIER90 package [48–51]. In order to have accurate density of states at the Fermi level, we have employed the WANNIER90 package [48–51] on top of our electronic structure calculations. Using the Bloch states for our relaxed 32 f.u. supercells, we extract the density of states on a very dense k mesh of $64\times\ 64\times 64$ points.

III. RESULTS

Charge disproportionation and insulating state at half doping. The next member in the doped nickelate phase diagram is the $n = 2$ member, which corresponds to a half-doped material. We thus inspect the structural and electronic properties of half-doped nickelates $La_{0.5}Sr_{0.5}NiO_2$ either as a superlattice (SL) with perfect layering between La and Sr layers along the c axis or a purely DSS, as well as in the "self-doped" RRP phase $La_3Ni_2O_6$. All systems possess a $Ni^{1.5+}$ $3d^{8.5}$ electronic configuration. After structural relaxation using a paramagnetic solution, we identify that the ground state of these materials is characterized, among all emergent lattice distortions, by a bond disproportionation mode B_{oc}—e.g., breathing of oxygen complexes—splitting the Ni sites into cations sitting in compressed (Ni_S) and extended (Ni_L) oxygen complexes and forming a layered checkerboard structure [Fig. 2(a)]. Using a symmetry mode analysis with respect to the primitive undistorted cell, we find sizable amplitudes of 0.0719, 0.0603, and 0.089 Å/NiO_2 motif in the SL, DSS, and RRP phases, respectively. The structural relaxations are associated with large energy gains with respect to the undistorted phases of -87, -53, and -32 meV/NiO_2 motif for the SL, DSS, and RRP phases, respectively.

The effect of the B_{oc} mode is to produce a clear asymmetry of the electronic structure associated with the two different Ni cations in the cell as inferred by the projected density of states (PDOS) on Ni_L and Ni_S cations [Fig. 2(b)] for the half-doped SL. The Fermi-level physics is dominated by Ni_L d states while Ni_S d states are pushed above E_F and separated from the Ni_L states. Furthermore, the O p orbitals do not bring a sizable contribution to the density of states (DOS) in this energy range, and the top of these states are, in fact, located 1 eV below the Fermi level. By looking at the partial charge density map originating from bands just at the Fermi level E_F, a charge ordering between Ni_L and Ni_S cations [Fig. 2(c)] is identified with Ni_L likely holding more electrons than Ni_S cations. The partial charge density maps also highlight the strong Mott character of these nickelates with negligible spread of the electronic structure on O atoms. The Mott character agrees with previous results on undoped materials [52–56]. In addition, the existence of a charge ordering is confirmed by our computed magnetic moments revealing that Ni_L sites bear a magnetic moment of $(0.99 \pm 0.05)\mu_B$ depending on the nature of the half-doped nickelate (i.e., SL, DSS, or RRP) and Ni_S sites have a moment of $(0.26 \pm 0.18)\mu_B$. The slight deviation from $0\mu_B$ for Ni_S sites comes from cation and/or spin disorders yielding a different local potential experienced by each Ni cation (see Fig. S3 in Supplemental Material [23]). Such a deviation was already observed in the DFT-PM state

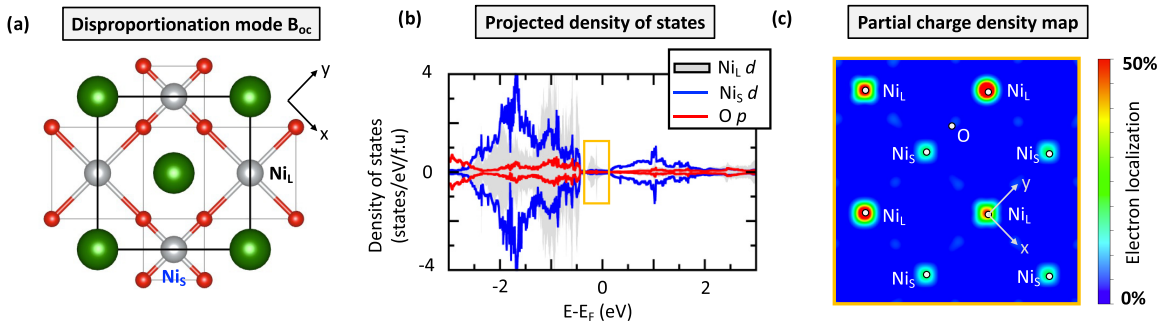

FIG. 2. Key properties of half-doped two-dimensional nickelates. (a) Bond disproportionation B_{oc} mode splitting Ni sites into Ni_L and Ni_S sitting in an extended and compressed oxygen complex, respectively. (b) Projected density of states on Ni_L (solid grey) and Ni_S (blue line) d states and O p states (red line) for the 50% doped superlattice. (c) Partial charge density map associated with bands just below the Fermi level indicated by the orange square in panel (b) in the half-doped superlattice.

of bond disproportionated materials in Ref. [29]. The clear magnetic moment asymmetry suggests that Ni_L cations are in a Ni^{1+} $3d^9$ configuration while Ni_S cations are in a Ni^{2+} $3d^8$ low-spin state.

Aiming at understanding how electrons localize in the ground state, we have built the Wannier functions (WFs) associated with the ground state of the 50% doped SL following the strategy presented in Ref. [57]. After minimizing the spread of the WFs, we infer that (i) all O p states are doubly occupied; (ii) for Ni_L cations all d orbitals are doubly occupied except for the $d_{x^2-y^2}$ orbital that holds a single electron; and (iii) for Ni_S cations all d orbitals are doubly occupied except the $d_{x^2-y^2}$ orbital that is empty (see Fig. S4 in Supplemental Material [23]). It confirms that the ground state of half-doped nickelates is associated with a charge order between Ni_L^{+} $3d^9$ and Ni_S^{2+} $3d^8$ low-spin cations. We conclude here that nickelates with $Ni^{1.5+}$ cations are prone to exhibit a bond disproportionation mode B_{oc} producing a charge ordering between Ni^{+} $3d^9$ and Ni^{2+} $3d^8$ cations.

As observed in the ABO_3 perovskites such as RNiO$_3$ (R = Lu-Pr,Y), ABiO$_3$ (A = Sr,Ba) or BaSbO$_3$ compounds [27,29,33,58,59], the effect of the B_{oc} mode is to open a band gap in the material. Our SCAN calculation predicts a weakly metallic state for the DSS, SL, and RPP with the PM order. However, this is inherent to DFT functionals that are local or semilocal operators of the noninteracting density matrix (e.g., LDA, GGA) that underestimate the band gap of compounds, including those of highly uncorrelated semiconductors. Using a more accurate but prohibitive HSE06 hybrid functional on short-range spin-ordered half-doped nickelates yields an insulating state (see Fig. S5 in Supplemental Material [23]).

In order to reveal the origin of the disproportionation effects, we examine the potential energy surface (PES) associated with the disproportionation mode B_{oc} in the SL, DSS, and RRP. To that end, we compute the total energy by freezing some amplitude of the B_{oc} mode starting from a high-symmetry undistorted cell (Fig. 3). In all three forms of half-doped nickelates, we identify a single-well potential whose minimum is shifted to nonzero amplitude of the B_{oc} mode. This indicates the existence of a force associated with an electronic instability acting to remove the electronic degeneracy of the $3d^{8.5}$ electronic configuration [44]. Furthermore, the instability is independent of the form of the structure (i.e., SL vs RRP) as well as of the order or disorder of A-site cations (i.e., SL vs DSS). This suggests that the formal occupancy of Ni $3d$ orbitals is the determining factor rather than the type

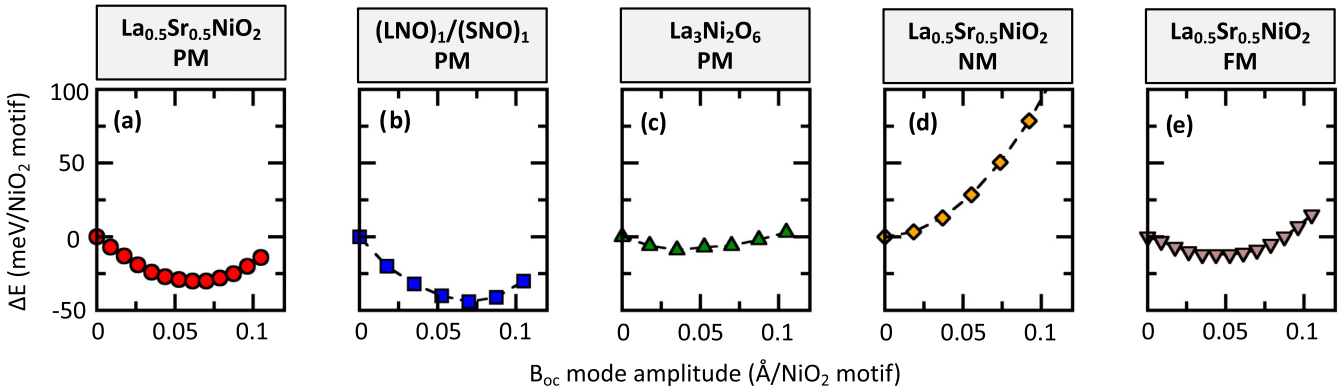

FIG. 3. Origin of disproportionation effects. Total energy gain ΔE (in meV/NiO$_2$ motif) as a function of the disproportionation B_{oc} mode amplitude (in Å/NiO$_2$ motif) for the half-doped nickelates using (a) a solid solution, (b) a superlattice, and (c) the $n = 2$ reduced Ruddlesden-Popper phases with paramagnetic order. Total energy gain (in meV/NiO$_2$ motif) as a function of the disproportionation B_{oc} mode amplitude (in Å/NiO$_2$ motif) for the half-doped nickelates using (d) NM and (e) FM order. The point at zero amplitude is set as the reference energy and corresponds to an undistorted cell.

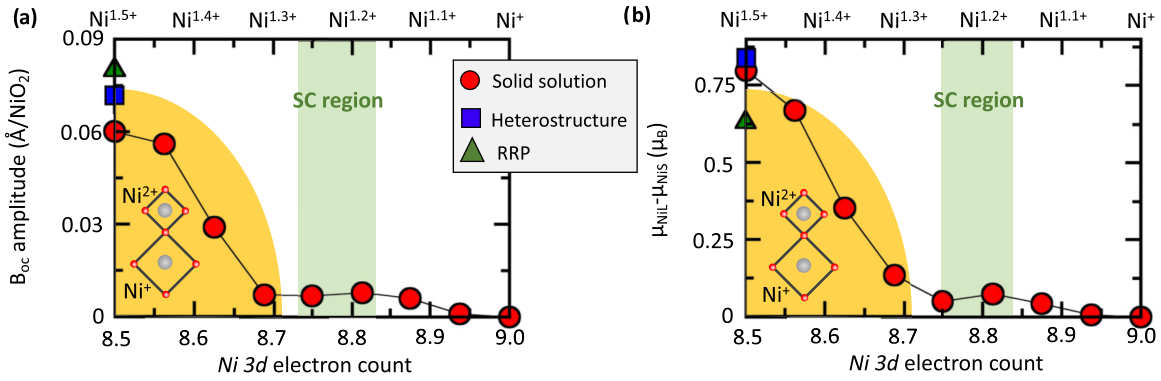

FIG. 4. Trend in disproportionation effect with doping content. (a) Amplitude (in Å/NiO_2 motif) associated with the B_{oc} bond disproportionation mode and (b) asymmetry of Ni_L and Ni_S magnetic moments as a function of Ni $3d$ electron count (lower scale) or Ni formal oxidation state (upper scale) for the fully relaxed ground-state superlattices (SL, solid blue squares), disordered solid solutions (DSS, solid red circles), and reduced Ruddlesden-Popper (RRP, solid green diamonds).

of layered structure adopted by the nickelate. The existence of an electronic instability associated with the unstable 1.5+ FOS of Ni cations is confirmed by a hybrid HSE06 calculation on an undistorted cell for which a d^8/d^9 charge ordering is more stable by 11.5 meV/f.u. than a $d^{8.5}$ occupancy of all Ni cations (see Fig. S6 in Supplemental Material [23]) and already opens a finite band gap in the system. We conclude here that the 1.5+ FOS of Ni cations is intrinsically unstable and is willing to disproportionate to more stable 1+ and 2+ FOSs in the ground state, thereby producing a charge ordering and a bond disproportionation mode B_{oc}.

The existence of a disproportionated insulating state at half doping is confirmed experimentally in $La_3Ni_2O_6$ (RRP $n = 2$) [60,61]. This was also predicted theoretically in Ref. [62]. Nevertheless, the existence of a half-doped infinitely layered phase is yet to be realized experimentally, although the phase stability may be questionable. However, should such a phase exist, it would be characterized by robust disproportionation effects of $Ni^{1.5+}$ cations.

Local spin formation is a key degree of freedom. Allowing spin degree of freedom and satisfying the basic Hund rule for Ni cations is crucial since a non-spin-polarized (NM) DFT calculation yields a single-well potential for B_{oc} whose minimum is centered at zero amplitude [Fig. 3(d)]. In contrast, all additional calculations performed with various long-range spin orders show the stabilization of the mode [see Fig. 3(e) for the ferromagnetic case]. This agrees with the existence of the breathing mode B_{oc} in the perovskite $RNiO_3$ phase that requires Hund's rule to be respected [33] (i.e., formation of local spins). Nevertheless, disproportionation effects are unrelated to correlation effects as is extensively discussed in Refs. [26,29,33,59]. Thus, along with predicting a solution at 1800 K/f.u. above a true PM solution, the NM approximation cannot capture the relevant structural lowering event associated with intrinsic electronic instabilities. It is thus irrelevant for studying the physics of nickelate superconductors.

Doping is a lever to suppress the charge-ordered insulating state. Having established the existence of disproportionation effects in half-doped nickelates and of an associated insulating phase, we now use this result as a starting point for studying the role of doping, i.e., hole doping starting from pristine $LaNiO_2$ material or electron doping starting from the half-doped $La_{0.5}Sr_{0.5}NiO_2$. The insulating starting point is similar between all forms of superconducting nickelates and a common point with the rest of the SC oxides. We now restrict the study to the DSS for convenience. To that end, we decrease the x value from 0.5 in $La_{1-x}Sr_xNiO_2$. We report in Fig. 4(a) the trend in bond disproportionation amplitude and magnetic moment asymmetry between Ni_L and Ni_S sites as a function of the nickel $3d$ electron count. We observe that starting from $Ni^{1.5+}$ cations ($x = 0.5$, Ni $3d^{8.5}$), the bond disproportionation amplitude extracted from a symmetry-mode analysis decreases until $x = 0.25$ (Ni $3d^{8.75}$). For $x < 0.25$, the mode is no longer stable. The same conclusions are raised using the magnetic moments difference displayed in Fig. 2(b) as well as with a long-range antiferromagnetic (AFM) order (see Fig. S7 in Supplemental Material [23]). The extinction of the disproportionation effects at $x = 0.25$ is reminiscent of the value at which superconductivity emerges experimentally in these compounds ($x \sim 0.2$ in DSS or $n = 5$ in RRP phases, corresponding to $Ni^{1.2+}$ $3d^{8.8}$ cations) [26]. We emphasize that although using a simpler E-type antiferromagnetic order (AFME) order compatible with the appearance of B_{oc} modes in oxides [44], the doped case at 37.5% ($3d^{8.625}$) is found to be insulating with the HSE06 DFT functional (see Fig. S8 in Supplemental Material [23]). We conclude here that doping acts to suppress the disproportionation effects—and the insulating phase—present in the half-doped nickelates.

Previous experimental works on the RRP phase with $n = 3$ revealed the existence of a charge-ordered state ($Ni^{1.33+}$ $3d^{8.66}$) [63–65], as well as an insulating character below 105 K [64,66], in agreement with our simulations. These findings are also supported by various theoretical works on the very same compounds, showing that the ground state is formed of Ni^+ and Ni^{2+} cations [67], in line with our results for the doped solid solution. Finally, an earlier theoretical work also revealed the propensity of the hole-doped $NdNiO_2$ to develop bond- and/or charge-ordered states [68]. We finally emphasize that oxygen-rich $NdNiO_{2+\delta}$ samples are also prone to exhibit charge orderings [69,70], highlighting the propensity of these doped infinitely layered nickelates to develop charge disproportionation effects.

Vicinity of a charge-ordered state is a prerequisite to superconductivity. We report in Fig. 5(a) the potential energy

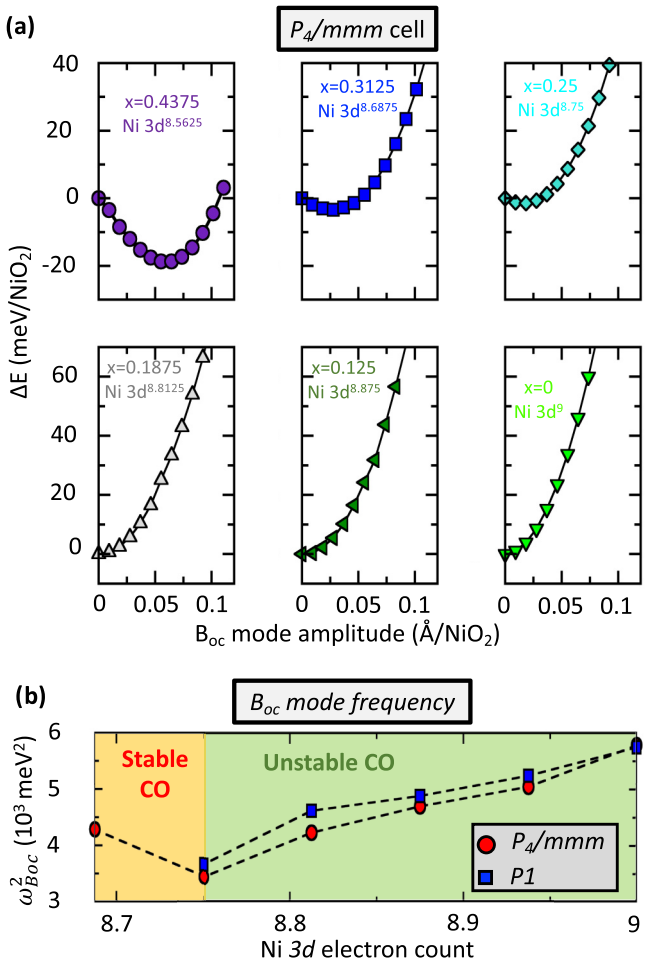

FIG. 5. Phonon frequency of the breathing mode B_{oc} upon doping. (a) Energy gain ΔE (in meV/NiO_2) associated with the breathing mode amplitude (in Å/NiO_2) starting from an undistorted *P4/mmm* cell for the disordered solution $La_{1-x}Sr_xNiO_2$ at different doping contents using the PM order. The reference energy is set to the value at zero B_{oc} mode amplitude. (b) Extracted squared B_{oc} phonon frequency (in meV^2) as a function of the Ni 3*d* electron count using the PM order within the undistorted *P*4/*mmm* (solid red squares) and real ground-state structure (solid blue circles).

surface of the B_{oc} mode starting from a high-symmetry cell for different doping contents for the DSS. Starting from the ideal doping content $x = 0.5$ (Ni $3d^{8.5}$), we see a shifted single well down to $x = 0.25$ (Ni $3d^{8.75}$), albeit the minimum is progressively displaced to lower mode amplitudes. Further decreasing x transforms the shifted single well to a single-well potential whose minimum is located at zero amplitude of the mode, indicating that the electronic instability associated with disproportionation effects is suppressed. At this stage, no more charge orderings—and hence semiconducting states—are expected. From $x = 0.25$ (Ni $3d^{8.75}$) to $x = 0$ (Ni $3d^9$), the curvature of the total energy as a function of the amplitude of displacement Q_{Boc} around the origin becomes steeper. Aiming at extracting the phonon frequency as a function of the doping content, we have fitted the PES of Fig. 5(a) as a function of Q_{Boc} with a polynomial expression of the form $\Delta E = \alpha(Q_{Boc} - Q_0)^2 + \beta(Q_{Boc} - Q_0)^4$, where Q_0 corresponds to the shift of the energy minimum induced by the force associated with electronic instability (see Methods for further details) and α and β are coefficients. Recalling that the harmonic contribution to the energy is $E_{\text{harm}} = \frac{1}{2}M\omega^2 Q^2_{Boc}$, where M is the mass of the moving atoms, we directly get that $\omega^2 = \frac{2\alpha}{M}$.

From the extracted squared B_{oc} phonon frequency as a function of doping content reported in Fig. 5(b), we see that ω^2_{Boc} strongly hardens from $x = 0.25$ to $x = 0$. Above $x = 0.25$, the B_{oc} mode frequency without the electronic instability would increase. It follows that the B_{oc} mode reaches its lowest frequency ω_{Boc} at the vicinity of a stable charge-ordered phase boundary, thereby maximizing the probability of its vibration in the material. In turn, it possibly favors the punctual formation of coupled electrons and holes on the lattice, i.e., the Cooper pairs. Although ω^2_{Boc} is rather low above $x = 0.25$, electrons and holes are localized in the lattice due to the finite stabilization of the B_{oc} mode induced by the electronic instability as discussed above in the paper, and *de facto* superconductivity cannot exist. A totally different picture is achieved with the NM approximation that provides a monotonous strengthening of ω_{Boc} with increasing the doping content (see Fig. S9 in Supplemental Material [23]), in addition to the absence of tendency toward charge disproportionation or ordering. Finally, we observe a very slight shift of ω^2_{Boc} to higher energies when considering the ground-state structure [Fig. 5(b)]. It signals the absence of significant couplings between the B_{oc} mode and other lattice distortions, in contrast to the usual behavior observed in $RNiO_3$ and $ABiO_3$ compounds [26,29,58]. We conclude here that the vicinity of a charge-ordered phase is a prerequisite for superconductivity in nickelates.

Nickelates are associated with a single-band system. We report in Fig. 6(a) the unfolded band structure of the DSS in the doped region for $La_{0.8125}Sr_{0.1875}NiO_2$ with the PM order. We observe a single-band system associated with the PM state in the SC region, described by a parabola centered at the A point: the (½, ½, ½) point of the Brillouin zone. This type of band structure is in sharp agreement with more complex dynamical mean field theory calculation [71] or the noncollinear PM DFT of Ref. [72]. The single-band system agrees with the experimental data analysis performed by Talantsev [73], who through different adjustments determined that the nickelate superconductivity should be described by a single band. Again, this result contradicts the band dispersion obtained with a NM approximation which produces a two-band system (see Fig. S10 in Supplemental Material [23]) due to the absence of Hund's rule.

From the band structure projected on different atom and orbital contributions reported in Fig. 6(b), the part of the parabola crossing the Fermi level along the *Z-R-A* path is dominated by Ni d_{xz}/d_{yz} orbitals, with smaller contributions from La states. This is in sharp agreement with spin-polarized DFT simulations performed by Lane *et al.* [74] and Zhang *et al.* [55,75] that identify a parabola centered at the *A* point in undoped $NdNiO_2$ compounds with d_{xz}/d_{yz} orbital character. The $d_{x^2-y^2}$ contributions that we observe do correspond to the impurity states introduced by the doping, and these orbitals are in fact located 1 eV below and 2 eV above E_F in the undoped samples.

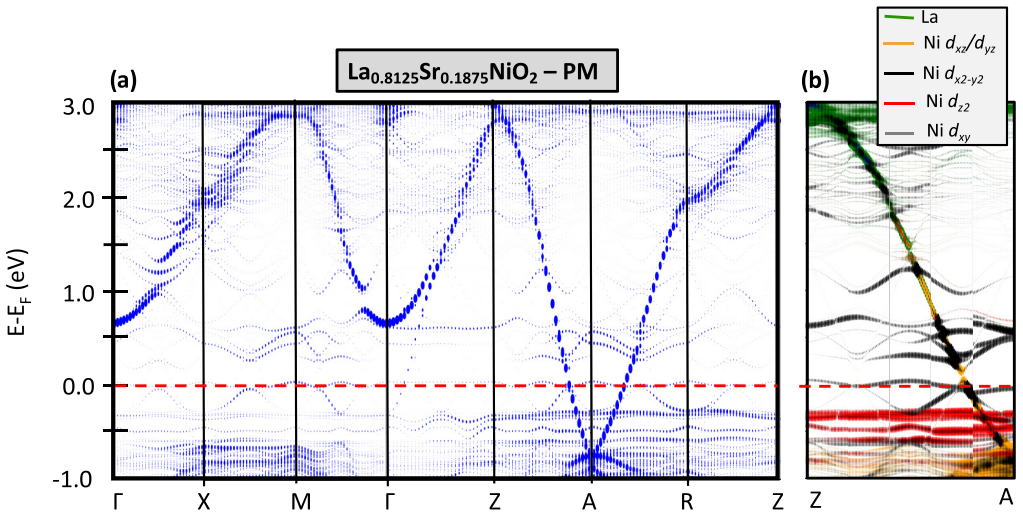

FIG. 6. Band dispersion associated with $La_{0.8125}Sr_{0.1875}NiO_2$. (a) Unfolded band structure to the primitive high-symmetry *P*4/*mmm* cell of $La_{0.8125}Sr_{0.1875}NiO_2$ with the PM order. Coordinates of the high-symmetry points are the following: Γ(0,0,0), *X*(1/2,0,0), *M*(1/2,1/2,0), *Z*(0,0,1/2), *R*(1/2,0,1/2), and *A*(1/2,1/2,1/2). (b) Bands dispersion along the *Z*-*A* path projected on all Ni d_{xy} (grey), $d_{xz}+d_{yz}$ (orange), d_{x2-y2} (black), and d_{z2} (red) states and total contribution from the *A* cation (green) states.

In order to track the existence of an interaction between the B_{oc} mode and the electronic structure, one can inspect band splitting along the *Z*-*A* path appearing in the band dispersion at various doping contents (see Fig. S11 in Supplemental Material [23])—bands dispersing along $(0,0,\frac{1}{2})-(\frac{1}{2},\frac{1}{2},\frac{1}{2})$ and compatible with the (½,½,0) B_{oc} mode symmetry (see Fig. S12 in Supplemental Material [23]). One notices that the band splitting progressively disappears upon adding electrons in the material. This is reminiscent of the situation observed in hole-doped bismuthates for which progressively doping the system transforms the material from a bond disproportionated insulator into a metal with a single parabola centered at the Γ point [26]. We emphasize that a gap also appears at quarter distance from the A point. This is due to the disorder introduced on spins in order to mimick a paramagnetic state as well as the cation subsitutions used to model the solid solution (see Fig. S13 in Supplemental Material [23]). Therefore, for a sufficiently electron-doped nickelate ($x \leqslant 0.25$), the DFT calculations suggest that there are no more interactions coming from the B_{oc} mode experienced by the electrons in the ground state.

At this stage, one may sum up the different observations raised by the DFT simulations. A strong electron-phonon coupling exists in the half-doped regime and originates from an unstable 1.5+ FOS of Ni cations that prefers to transform into more stable 1+ and 2+ FOSs in the ground state. It results in electron localization with the appearance of Ni^{+} ($3d^9$)/Ni^{2+} ($3d^8$ low spin) charge ordering that is accompanied by a Ni-O bond ordering (BO) through a breathing of oxygen complexes B_{oc} distortion. It ultimately results in an insulating phase. Electron doping the half-doped case alters the electron-phonon coupling albeit preventing the stabilization of a CO and BO until $x = 0.25$ in $La_{1-x}Sr_xNiO_2$ compounds. For $x < 0.25$, the electron-phonon coupling associated with the CO and BO is sufficiently weakened so that no more electron localization is stabilized nor are Ni-O bond orderings. One is then left with a metallic state. Although weakened by electron doping, one may thus question if the electron-phonon coupling remains sufficiently large in the metallic regime for mediating the formation of Cooper pairs and producing the dome of T_c versus doping content. We inspect this possibility in detail in the following sections.

Superconducting quantities. The electron-phonon coupling (EPC) is proportional to the inverse of the frequency square of modes, to the REPME (labeled *D*) squared, and to the density of states at the Fermi level, $N(E_F)$ (i.e., $\lambda \propto N(E_F)\frac{D^2}{\omega^2}$; see Methods). Figure 7(a) displays the evolution of $N(E_F)$ as a function of *x* extracted using a very dense *k* mesh. The DOS at E_F diminishes upon hole doping $LaNiO_2$ until it drops at $x = 0.25$ ($3d^{8.75}$). The behavior between $x = 0$ ($3d^9$) and $x = 0.1875$ ($3d^{8.8125}$) agrees with expectation from a free electron system for which DOS evolves as $\sqrt{E}$.

We extract the REPME induced by the bond disproportionation mode B_{oc}. To that end, we add an arbitrary amplitude Q_{Boc} of 0.1106 Å/NiO_2 motif of the B_{oc} mode, i.e., a displacement of 0.0553 Å per O atom in the ground-state DSS structure of $La_{1-x}Sr_xNiO_2$ ($x = 0$ to 0.25). We identify in the band structure a gap opening ΔE_k of 0.64 eV along the *Z*-*A* path for $x = 0.1875$ (see Fig. S14 in Supplemental Material [23]). The B_{oc} mode induces a REPME $D = \Delta E_k/Q_{Boc} = 5.12\,\text{eV Å}^{-1}$ (see Methods). We checked that ΔE_k scales linearly with *u*; i.e., *D* is constant for these amplitudes of vibration (see Fig. S15 in Supplemental Material [23]). We report in Fig. 7(b) the REPME as a function for the doping content. It describes a bell-shaped evolution whose maximal value is at $x = 0.1875$ ($3d^{8.8125}$). This hints at the maximal T_c observed experimentally for such doping content ($x = 0.2$, $3d^{8.8}$). Using the NM approximation as in Ref. [15], we end up with a totally different behavior with a monotonously increasing *D* value with increasing *x* (see Fig. S9 in Supplemental Material [23]). It nevertheless shows that extracting quantities within pristine compounds is not appropriate because doping acts on the REPME value. However, our SCAN-DFT simulations give a lower value for *D*. We have fitted the evolution of

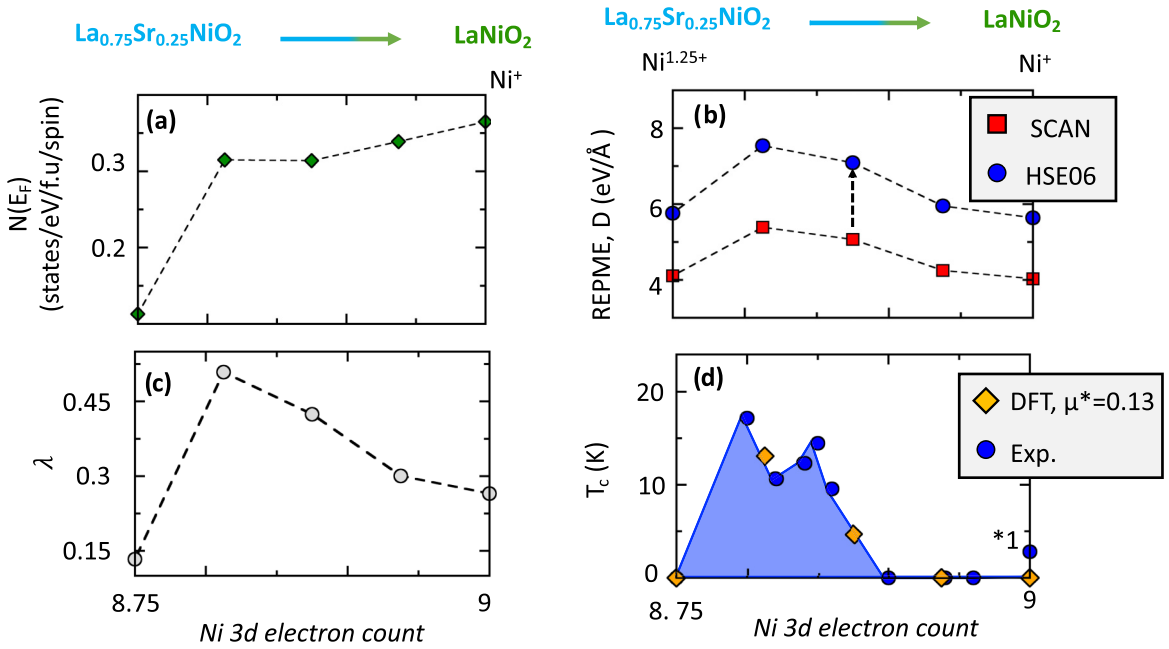

FIG. 7. Superconducting properties of doped nickelates. (a) Density of states $N(E_F)$ (states/eV/f.u./spin channel) of the DSS nickelates upon Sr doping. (b) Reduced electron-phonon matrix element (REPME, in eV Å^{-1}) as a function of the Sr doping content obtained with SCAN (solid red squares) and rescaled by the HSE06 functional (solid blue circles). (c) Computed electron-phonon coupling constant (no units) obtained from REPME, $N(E_F)$ and ω_{Boc}. (d) Computed critical temperature T_c (in kelvin) from our DFT simulations using usual screened Coulomb potential $\mu^* = 0.13$ (solid orange diamonds) and $\mu = 0.15$ (solid orange inverted triangles). Experimental values (solid blue circles) are extracted from Ref. [6]. *1: The value at $x = 0$ presents some uncertainty since the measurement of Ref. [6] was limited to 2 K and the resistivity did not reach zero.

the D parameter between heterostructures at $x = 0.25$, 0.125, and 0.0 in order to extract the enhancement of ΔE_k produced by an HSE06 calculation over a SCAN calculation (see Fig. S16 in Supplemental Material [23]). We observe a global enhancement of 40% of the SCAN value. We thus rescale our ΔE_k on the PM $La_{1-x}Sr_xNiO_2$ by 1.4 in order to better describe this property [Fig. 7(b)].

Using the $N(E_F)$, ω^2_{Boc}, and REPMEs with the HSE06 correction, we can compute the electron-phonon coupling for each doping content induced by the sole breathing mode [Fig. 7(c)]. As one can see, λ is dominated by the D^2 factor by describing a bell-shaped evolution with a coupling constant reaching 0.51 at $x = 0.1875$ ($3d^{8.8125}$) of Sr doping content—in the charge-ordered insulating phases, DOS at E_F is supposedly zero and, hence, there is no superconductivity. The value of $\lambda = 0.51$ is very close to the value extracted by the experimental analysis of Talantsev that identified λ between 0.58 and 0.60 in the optimally doped nickelates ($R_{0.8}Sr_{0.2}NiO_2$, $3d^{8.8}$) [76].

Using the McMillan equation [32] with the screened Coulomb potential μ^* of 0.13 estimated from experimental data analysis of Talantsev [76] and assuming that ω_{Boc} is the characteristic energy scale for the interacting phonons contributing to the SC mechanism, our model yields a T_c evolution as a function of Sr doping content, in sharp agreement with the experimental values available in the literature [6] [Fig. 7(d)]. Numbers may of course be improved by involving higher-level DFT functionals such as hybrid DFT or a full electron-phonon calculation implying all phonon modes; this is, however, not affordable for a 32 f.u. with spin and cation disorders, and no electron-phonon calculation technics allowing spin polarization is available to date, to the best of our knowledge. However, the T_c trend is already well captured by the SCAN functional, thereby suggesting that the bond disproportionation phonon mode is the dominating factor behind the superconducting properties of nickelates.

The phonon-driven mechanism is not incompatible with the experimental gap symmetry. The superconducting gap symmetry is found to be nontrivial experimentally [77–79], pointing to an anisotropic gap with several pairing symmetries. This deviation from the most simple BCS isotropic *s*-wave pairing symmetry is usually understood to be a signature of nonconventional pairing. However, phonon-mediated superconductivity does not impose any pairing symmetry: a phonon-mediated mechanism and an anisotropic pairing can exist since the electron-phonon coupling is momentum dependent. This has been highlighted in nickelates [80] as well as in cuprates [81]. Notably the pairing symmetry can be even nodal within a phonon-mediated scheme and the evaluation of the critical temperature T_c can be done with the same BCS-type equation without loss of generality [82]. Thus, from the point of view of calculating the critical temperature, one may be able to evaluate with a good degree of accuracy using the usual *s*-wave equations for superconductors with any paring symmetry. From the point of view of the pairing symmetry, we can mainly refer to early theoretical works pointing to an *s*-wave pairing symmetry to explain properly the experimental data of the London penetration depth and the superfluid current density [73]. This has been also highlighted in some of the experimental works [77] and in other global studies for

several superconducting samples [76]. We can conclude here that our proposed model does not contradict the experimental data regarding the pairing symmetry and, although we do not propose a complete picture of it, a *s*-wave phonon-mediated scheme seems to be plausible and the easiest explanation.

IV. DISCUSSION

The physical behavior and key quantities extracted with our DFT simulations in nickelates are reminiscent of trends in doping and superconducting properties of bismuth oxide superconductors [24,26]. Most notably, in both families, doping is a lever to progressively suppress an instability toward disproportionation effects producing an insulating state and to drive the material to the vicinity of a charge-ordered state. Moreover, both compounds are single-band system superconductors. Our calculations show that nickelates are phonon-driven superconductors and we thus conclude that they bear more similarities with bismuth and antimony oxide superconductors than with cuprates. We emphasize that a recent theoretical work also identifies an electron-phonon coupling mechanism albeit originating from distinct phonon modes [28]. This discrepancy could originate from the non-spin-polarized (NM) approximation used in Ref. [28]. As we show here, the NM approximation (i) fails to describe phonons strongly coupled to local spin formations and (ii) produces a two-band system instead of a single-band system within a real PM treatment. Consequently, a full electron-phonon calculation with local spin formation might be the desired approach to clarify these details. This is, however, not affordable since it would require full spin-polarized calculation of the electron-phonon interaction which is not, to the best of our knowledge, implemented in any DFT code.

From our results, it appears that there are three important ingredients to reach superconductivity in nickelates: (i) the phonon has to be soft enough so that it can get locally excited to produce attraction between the electrons, (ii) it has to produce a sufficiently large electron-phonon coupling constant, and (iii) one needs a sufficiently large density of states at E_F to get a large EPC. Since DFT that only treats static mean-field correlation effects is a sufficient platform to get relevant quantities and information on the superconducting mechanism, it suggests that dynamical correlation effects as codified by the Hubbard model play a marginal role in the physics of nickelates. However, we do not claim that any other forms of correlations are not important since allowing local spin formation is an essential factor to identify the breathing distortion.

Finally, undoped materials are not necessarily a good starting point for understanding trends in doping effects and superconducting properties in oxides. The search for potential electronic and structural instabilities in the doped phase diagram appears as a critical aspect. Once the proper starting point is established, the identified phonon-driven mechanism common between nickel oxide and bismuth oxide superconductors therefore calls for new investigations of doping effects from the point of view of structural distortions and intrinsic electronic instabilities rather than from the strict point of view of electron correlation in other oxide superconductors.

ACKNOWLEDGMENTS

This work has received financial support from the CNRS through the MITI interdisciplinary programs under the project SuNi and through the ANR SUPERNICKEL. Authors acknowledge access granted to HPC resources of Criann through the Projects No. 2020005 and No. 2007013 and of Cines through the DARI Project No. A0080911453. L.I. acknowledges the funding from the Ile de France region and the European Union's Horizon 2020 research and innovation programme under the Marie Sklodowska-Curie Grant Agreement No. 21004513 (DOPNICKS project).

[1] L. N. Cooper, Phys. Rev. **104**, 1189 (1956).
[2] J. G. Bednorz and K. A. Müller, Z. Phys. B Condens. Matter. **64**, 189 (1986).
[3] V. I. Anisimov, D. Bukhvalov, and T. M. Rice, Phys. Rev. B **59**, 7901 (1999).
[4] J. Chaloupka and G. Khaliullin, Phys. Rev. Lett. **100**, 016404 (2008).
[5] D. Li, K. Lee, B. Y. Wang, M. Osada, S. Crossley, H. R. Lee, Y. Cui, Y. Hikita, and H. Y. Hwang, Nature (London) **572**, 624 (2019).
[6] M. Osada, B. Y. Wang, B. H. Goodge, S. P. Harvey, K. Lee, D. Li, L. F. Kourkoutis, and H. Y. Hwang, Adv. Mater. **33**, 2104083 (2021).
[7] M. Osada, B. Y. Wang, B. H. Goodge, K. Lee, H. Yoon, K. Sakuma, D. Li, M. Miura, L. F. Kourkoutis, H. Y. Hwang, M. Osada, and H. Y. Hwang, Nano Lett. **20**, 5735 (2020).
[8] S. Zeng, C. Li, L. E. Chow, Y. Cao, Z. Zhang, and C. S. Tang, Sci. Adv. **8**, eabl9927 (2022).
[9] G. A. Pan, D. F. Segedin, H. LaBollita, Q. Song, E. M. Nica, B. H. Goodge, A. T. Pierce, S. Doyle, S. Novakov, D. C. Carrizales, A. T. N'Diaye, P. Shafer, H. Paik, J. T. Heron, J. A. Mason, A. Yacoby, L. F. Kourkoutis, O. Erten, C. M. Brooks, A. S. Botana, and J. A. Mundy, Nat. Mater. **21**, 160 (2021).
[10] Y. Maeno, H. Hashimoto, K. Yoshida, S. Nishizaki, T. Fujita, J. G. Bednorz, and F. Lichtenberg, Nature (London) **372**, 532 (1994).
[11] Y. J. Yan, M. Q. Ren, H. C. Xu, B. P. Xie, R. Tao, H. Y. Choi, N. Lee, Y. J. Choi, T. Zhang, and D. L. Feng, Phys. Rev. X **5**, 041018 (2015).
[12] Y. K. Kim, N. H. Sung, J. D. Denlinger, and B. J. Kim, Nat. Phys. **12**, 37 (2016).
[13] X. Zhou, X. Zhang, J. Yi, P. Qin, Z. Feng, P. Jiang, Z. Zhong, H. Yan, X. Wang, H. Chen, H. Wu, X. Zhang, Z. Meng, X. Yu, M. B. H. Breese, J. Cao, J. Wang, C. Jiang, and Z. Liu, Adv. Mater. **34**, 2106117 (2022).
[14] F. Lechermann, Phys. Rev. B **101**, 081110 (2020).
[15] Y. Nomura, M. Hirayama, T. Tadano, Y. Yoshimoto, K. Nakamura, and R. Arita, Phys. Rev. B **100**, 205138 (2019).
[16] M. Hirayama, T. Tadano, Y. Nomura, and R. Arita, Phys. Rev. B **101**, 075107 (2020).
[17] V. Christiansson, F. Petocchi, and P. Werner, Phys. Rev. B **107**, 045144 (2023).

[18] T. Y. Xie, Z. Liu, C. Cao, Z. F. Wang, J. L. Yang, and W. Zhu, Phys. Rev. B **106**, 035111 (2022).

[19] Z. Liu, Z. Ren, W. Zhu, Z. Wang, and J. Yang, npj Quantum Mater. **5**, 31 (2020).

[20] P. Adhikary, S. Bandyopadhyay, T. Das, I. Dasgupta, and T. Saha-Dasgupta, Phys. Rev. B **102**, 100501(R) (2020).

[21] F. Bernardini, V. Olevano, and A. Cano, Phys. Rev. Res. **2**, 013219 (2020).

[22] M. Hepting, D. Li, C. J. Jia, H. Lu, E. Paris, Y. Tseng, X. Feng, M. Osada, E. Been, Y. Hikita, Y. D. Chuang, Z. Hussain, K. J. Zhou, A. Nag, M. Garcia-Fernandez, M. Rossi, H. Y. Huang, D. J. Huang, Z. X. Shen, T. Schmitt, H. Y. Hwang, B. Moritz, J. Zaanen, T. P. Devereaux, and W. S. Lee, Nat. Mater. **19**, 381 (2020).

[23] See Supplemental Material at http://link.aps.org/supplemental/10.1103/PhysRevMaterials.8.064801 for additional data supporting the conclusions drawn in the main manuscript.

[24] A. W. Sleight, Phys. C Supercond. Appl. **514**, 152 (2015).

[25] C. H. P. Wen, H. C. Xu, Q. Yao, R. Peng, X. H. Niu, Q. Y. Chen, Z. T. Liu, D. W. Shen, Q. Song, X. Lou, Y. F. Fang, X. S. Liu, Y. H. Song, Y. J. Jiao, T. F. Duan, H. H. Wen, P. Dudin, G. Kotliar, Z. P. Yin, and D. L. Feng, Phys. Rev. Lett. **121**, 117002 (2018).

[26] J. Varignon, Npj Comput. Mater. **9**, 30 (2023).

[27] M. Kim, G. M. McNally, H. H. Kim, M. Oudah, A. S. Gibbs, P. Manuel, R. J. Green, R. Sutarto, T. Takayama, A. Yaresko, U. Wedig, M. Isobe, R. K. Kremer, D. A. Bonn, B. Keimer, and H. Takagi, Nat. Mater. **21**, 627 (2022).

[28] Z. Li and S. G. Louie, arXiv:2210.12819.

[29] J. Varignon, M. Bibes, and A. Zunger, Nat. Commun. **10**, 1658 (2019).

[30] Z. P. Yin, A. Kutepov, and G. Kotliar, Phys. Rev. X **3**, 021011 (2013).

[31] J. M. An and W. E. Pickett, Phys. Rev. Lett. **86**, 4366 (2001).

[32] P. B. Allen and R. C. Dynes, Phys. Rev. B **12**, 905 (1975).

[33] J. Varignon, M. Bibes, and A. Zunger, Phys. Rev. B **100**, 035119 (2019).

[34] J. Sun, A. Ruzsinszky, and J. P. Perdew, Phys. Rev. Lett. **115**, 036402 (2015).

[35] L. Iglesias, M. Bibes, and J. Varignon, Phys. Rev. B **104**, 035123 (2021).

[36] A. A. Carrasco Alvarez, M. Bibes, W. Prellier, and J. Varignon, Phys. Rev. B **107**, 115109 (2023).

[37] A. V. Krukau, O. A. Vydrov, A. F. Izmaylov, and G. E. Scuseria, J. Chem. Phys. **125**, 224106 (2006).

[38] K. Pokharel, C. Lane, J. W. Furness, R. Zhang, J. Ning, B. Barbiellini, R. S. Markiewicz, Y. Zhang, A. Bansil, and J. Sun, Npj Comput. Mater. **8**, 31 (2022).

[39] J. K. Perry, J. Tahir-Kheli, and W. A. Goddard, Phys. Rev. B **65**, 144501 (2002).

[40] A. Van de Walle, M. Asta, and G. Ceder, Calphad Comput. Coupling Phase Diagrams Thermochem. **26**, 539 (2002).

[41] A. Zunger, S.-H. Wei, L. G. Ferreira, and J. E. Bernard, Phys. Rev. Lett. **65**, 353 (1990).

[42] B. J. Campbell, H. T. Stokes, D. E. Tanner, and D. M. Hatch, J. Appl. Crystallogr. **39**, 607 (2006).

[43] ISOTROPY Software Suite, iso.byu.edu. https://iso.byu.edu/iso/isodistort_version5.6.1/isodistort.php.

[44] J. Varignon, O. I. Malyi, and A. Zunger, Phys. Rev. B **105**, 165111 (2022).

[45] G. Kresse and J. Hafner, Phys. Rev. B **47**, 558 (1993).

[46] G. Kresse and J. Furthmüller, Comput. Mater. Sci. **6**, 15 (1996).

[47] P. E. Blöchl, Phys. Rev. B **50**, 17953 (1994).

[48] A. A. Mostofi, J. R. Yates, Y.-S. Lee, I. Souza, D. Vanderbilt, and N. Marzari, Comput. Phys. Commun. **178**, 685 (2008).

[49] N. Marzari and D. Vanderbilt, Phys. Rev. B **56**, 12847 (1997).

[50] I. Souza, N. Marzari, and D. Vanderbilt, Phys. Rev. B **65**, 035109 (2001).

[51] G. Pizzi, V. Vitale, R. Arita, S. Blügel, F. Freimuth, G. Géranton, M. Gibertini, D. Gresch, C. Johnson, T. Koretsune, J. Ibañez-Azpiroz, H. Lee, J. M. Lihm, D. Marchand, A. Marrazzo, Y. Mokrousov, J. I. Mustafa, Y. Nohara, Y. Nomura, L. Paulatto, S. Poncé, T. Ponweiser, J. Qiao, F. Thöle, S. S. Tsirkin, M. Wierzbowska, N. Marzari, D. Vanderbilt, I. Souza, A. A. Mostofi, and J. R. Yates, J. Phys. Condens. Matter **32**, 165902 (2020).

[52] Z. Chen, M. Osada, D. Li, E. M. Been, S. Di Chen, M. Hashimoto, D. Lu, S. K. Mo, K. Lee, B. Y. Wang, F. Rodolakis, J. L. McChesney, C. Jia, B. Moritz, T. P. Devereaux, H. Y. Hwang, and Z. X. Shen, Matter **5**, 1806 (2022).

[53] B. H. Goodge, D. Li, K. Lee, M. Osada, B. Y. Wang, G. A. Sawatzky, H. Y. Hwang, and L. F. Kourkoutis, Proc. Natl. Acad. Sci. USA **118**, e2007683118 (2021).

[54] M. Y. Choi, K. W. Lee, and W. E. Pickett, Phys. Rev. B **101**, 020503(R) (2020).

[55] R. Zhang, C. Lane, B. Singh, J. Nokelainen, B. Barbiellini, R. S. Markiewicz, A. Bansil, and J. Sun, Commun. Phys. **4**, 118 (2021).

[56] M. Y. Choi, W. E. Pickett, and K. W. Lee, Phys. Rev. Res. **2**, 033445 (2020).

[57] J. Varignon, M. N. Grisolia, J. Íñiguez, A. Barthélémy, and M. Bibes, npj Quantum Mater. **2**, 21 (2017).

[58] A. Mercy, J. Bieder, J. Íñiguez, and P. Ghosez, Nat. Commun. **8**, 1677 (2017).

[59] G. M. Dalpian, Q. Liu, J. Varignon, M. Bibes, and A. Zunger, Phys. Rev. B **98**, 075135 (2018).

[60] V. V. Poltavets, K. A. Lokshin, S. Dikmen, M. Croft, T. Egami, and M. Greenblatt, J. Am. Chem. Soc. **128**, 9050 (2006).

[61] K. A. Lokshin, D. Mitchell, M. V. Lobanov, V. Struzhkin, and T. Egami, ECS J. Solid State Sci. Technol. **11**, 044008 (2022).

[62] V. Pardo and W. E. Pickett, Phys. Rev. B **83**, 245128 (2011).

[63] Y. Shen, J. Sears, G. Fabbris, J. Li, J. Pelliciari, I. Jarrige, X. He, I. Božović, M. Mitrano, J. Zhang, J. F. Mitchell, A. S. Botana, V. Bisogni, M. R. Norman, S. Johnston, and M. P. M. Dean, Phys. Rev. X **12**, 011055 (2022).

[64] J. Zhang, Y. S. Chen, D. Phelan, H. Zheng, M. R. Norman, and J. F. Mitchell, Proc. Natl. Acad. Sci. USA **113**, 8945 (2016).

[65] X. Chen, H. Zheng, D. P. Phelan, H. Zheng, S. H. Lapidus, M. J. Krogstad, R. Osborn, S. Rosenkranz, and J. F. Mitchell, Chem. Mater. **34**, 4560 (2022).

[66] V. V. Poltavets, K. A. Lokshin, A. H. Nevidomskyy, M. Croft, T. A. Tyson, J. Hadermann, G. Van Tendeloo, T. Egami, G. Kotliar, N. Aproberts-Warren, A. P. Dioguardi, N. J. Curro, and M. Greenblatt, Phys. Rev. Lett. **104**, 206403 (2010).

[67] A. S. Botana, V. Pardo, W. E. Pickett, and M. R. Norman, Phys. Rev. B **94**, 081105(R) (2016).

[68] K. G. Slobodchikov and I. V. Leonov, Phys. Rev. B **106**, 165110 (2022).

[69] G. Krieger, L. Martinelli, S. Zeng, L. E. Chow, K. Kummer, R. Arpaia, M. Moretti Sala, N. B. Brookes, A. Ariando, N. Viart,

M. Salluzzo, G. Ghiringhelli, and D. Preziosi, Phys. Rev. Lett. **129**, 027002 (2022).
[70] A. Raji, G. Krieger, N. Viart, D. Preziosi, J.-P. Rueff, and A. Gloter, Small **19**, 2304872 (2023).
[71] H. Chen, A. Hampel, J. Karp, F. Lechermann, and A. J. Millis, Front. Phys. **10**, 835942 (2022).
[72] R. Jiang, Z.-J. Lang, T. Berlijn, and W. Ku, Phys. Rev. B **108**, 155126 (2023).
[73] E. F. Talantsev, Results Phys. **17**, 103118 (2020).
[74] C. Lane, R. Zhang, B. Barbiellini, R. S. Markiewicz, A. Bansil, J. Sun, and J. X. Zhu, Commun. Phys. **6**, 90 (2023).
[75] R. Zhang, C. Lane, J. Nokelainen, B. Singh, B. Barbiellini, R. S. Markiewicz, A. Bansil, and J. Sun, arXiv:2207.00184.
[76] E. F. Talantsev, J. Appl. Phys. **134**, 113904 (2023).
[77] L. E. Chow, S. K. Sudheesh, P. Nandi, S. W. Zeng, Z. T. Zhang, X. M. Du, Z. S. Lim, E. E. M. Chia, and A. Ariando, arXiv:2201.10038.
[78] Q. Gu, Y. Li, S. Wan, H. Li, W. Guo, H. Yang, Q. Li, X. Zhu, X. Pan, Y. Nie, and H. H. Wen, Nat. Commun. **11**, 6027 (2020).
[79] S. P. Harvey, B. Y. Wang, J. Fowlie, M. Osada, K. Lee, Y. Lee, D. Li, and H. Y. Hwang, arXiv:2201.12971.
[80] X. Sui, J. Wang, X. Ding, K.-J. Zhou, L. Qiao, H. Lin, and B. Huang, Phys. Rev. B **107**, 075159 (2023).
[81] T. P. Devereaux, T. Cuk, Z. X. Shen, and N. Nagaosa, Phys. Rev. Lett. **93**, 117004 (2004).
[82] P. W. Anderson and P. Morel, Phys. Rev. **123**, 1911 (1961).